



Effectiveness of the dispersion of iron nanoparticles within micropores and mesopores of activated carbon for Rhodamine B removal in wastewater by the heterogeneous Fenton process

Bi Gouessé Henri Briton¹ · Laurent Duclaux² · Yohan Richardson³ · Kouassi Benjamin Yao¹ · Laurence Reinert² · Yasushi Soneda⁴

Received: 27 February 2019 / Accepted: 23 September 2019 / Published online: 30 September 2019
© The Author(s) 2019

Abstract

Iron-based nanoparticles were formed in the pores of a micro- and mesoporous activated carbon made from banana spike by the impregnation of iron sulfate at various ratios and further pyrolysis, in order to prepare three catalysts AC@Fe/1, AC@Fe/2, AC@Fe/3 having iron mass contents of 1.6%, 2.2% and 3.3%, respectively. The pore size distributions, transmission electron microscope observations and X-ray photoelectron spectroscopy analyses have revealed that iron-based nanoparticles of 1–50 nm diameter, containing O and P, are located mainly in the supermicropores and mesopores of the activated carbon. Catalysts have been used to remove Rhodamine B in an aqueous solution by the heterogeneous Fenton process. AC@Fe/3 catalyst has allowed achieving 93% of solution discoloration compared to 87.4% for AC@Fe/2 and 78.5% for AC@Fe/1 after 180 min in batch reaction. The catalytic efficiency of AC@Fe/3 is attributed to the highest dispersion of the iron-based nanoparticles in the activated carbon porosity. The effects of hydrogen peroxide and initial dye concentration, pH, catalyst amount and temperature on the Rhodamine B removal kinetics catalyzed by AC@Fe/3 were studied. This catalyst showed remarkable performances of the Rhodamine B mineralization and possibility of recycling.

Keywords Heterogeneous catalyst · Fenton process · Rhodamine B · Discoloration · Degradation · Kinetics

Electronic supplementary material The online version of this article (<https://doi.org/10.1007/s13201-019-1047-0>) contains supplementary material, which is available to authorized users.

✉ Bi Gouessé Henri Briton
britonbig@yahoo.fr

- ¹ Laboratoire de Procédés Industriels de Synthèse, de l'Environnement et des Energies Nouvelles (LAPISEN), Institut National Polytechnique Félix Houphouët Boigny, BP 1093, Yamoussoukro, Ivory Coast
- ² Laboratoire de Chimie Moléculaire et de l'Environnement (LCME), Université Savoie Mont Blanc, 73000 Chambéry, France
- ³ Laboratoire Biomasse Energie et Biocarburants (LBEB), Institut International d'ingénierie de l'eau et de l'Environnement, 01 BP 594, Ouagadougou 01, Burkina Faso
- ⁴ Energy Technology Research Institute, National Institute of Advanced Industrial Science and Technology, 16-1 Onogawa, Tsukuba, Ibaraki 305-8569, Japan

Introduction

The textile industry occupies a very important place in the world economy. To satisfy customers and increase the turnover, very stable synthetic dyes are used to preserve the color of the textiles against the effect of ultraviolet sun irradiation and the oxidation from detergent products. These synthetic dyes which are generally high molecules of molar mass, and containing several benzene nuclei (Song and Li 2009), can create harmful impact on the environment (El Bouraie and El Din 2016), particularly on surface waters and soils, because they are resistant to biological degradation (Imran et al. 2015). Several textile industries from the developing countries which are unable to treat process wastewater often get rid of them directly, thus polluting the surface waters (Dellamatrice et al. 2016; Rajasimman et al. 2017).

In order to treat the textile effluents and degrade the harmful dyes, research efforts have concerned the treatment techniques based on advanced oxidation processes at both laboratory and industrial scales (Baldrian et al. 2006; Yu et al. 2016). These processes such as photocatalysis using

TiO₂/UV, electro-oxidation, catalytic ozonation, sono-chemistry and homogeneous Fenton are based on the production of very oxidant radical species able to reduce the contaminants in biodegradable compounds or even in CO₂ and H₂O (Ahmadi et al. 2017; Garza-Campos et al. 2016). Among these processes, several are expensive, while the Fenton process is financially more attractive because it requires for its implementation only the use of Fe²⁺ or Fe³⁺/H₂O₂ reagents to generate OH[•] hydroxyl radicals (De Lima Perini et al. 2013; Wang et al. 2014). In order to avoid the recovery of iron ions in the treated effluent, studies have focused on the supporting of iron nanoparticles on porous materials (silica, zeolite, graphene oxide, clay, activated carbon, etc.) (Diao et al. 2017; Guo et al. 2017; Liu et al. 2013; Rache et al. 2014) or on the use of materials (laterite, graphite waste) (Cuiping et al. 2012; Khataee et al. 2015; Wang 2011) naturally rich in iron.

Recent work has been devoted to the development of heterogeneous catalysts by co-precipitation of iron oxide nanoparticles on porous materials to form iron oxide deposit (Hassan et al. 2016; Kakavandi et al. 2016; Yu et al. 2016). This iron oxide deposit may considerably reduce the specific surface area and pore volume of the support (Yu et al. 2016). In fact, the low accessibility of the dyes to the pores by adsorption in the Fenton reaction can slow down the degradation speed (Yu et al. 2016). By contrast, a rational occupation of the pores of support and a good dispersion of the iron nanoparticles could raise the efficiency of the heterogeneous catalyst (Duarte et al. 2012; Liu et al. 2017). In an ideal catalyst, the surfaces defined by the micropores and mesopores must be accessible both to the hydrogen peroxide (H₂O₂) for the production of hydroxyl radicals and to pollutants submitted to the degradation. The development of an appropriate supported catalyst makes possible the reduction in the distance between the adsorbed pollutant and the produced hydroxyl radicals which have only a half-life time of a few nanoseconds and a migration distance of about one micrometer (Bačić and Mojović 2005).

Some authors have recently reported the efficient catalytic activity of iron oxide nanoparticles highly dispersed within porous materials for the removal of pollutants (Castro et al. 2009; Mahy et al. 2014; Mazilu et al. 2017). Among the porous materials able to support iron nanoparticles, activated carbon has interesting properties in terms of high surface area, surface chemistry, stability in acidic or basic media and very wide spectrum of pore size distribution (micropores, mesopores and macropores) according to its activation process type (El-Shafey et al. 2016). For example, the work of Nidheesh and Rajan (2016) reported on the degradation of Rhodamine B in an aqueous solution by the heterogeneous Fenton process using commercial activated carbon to support iron oxide nanoparticles. Generally, activated carbon as a catalytic support is used as a

powder and crushing into smaller fraction damages some of the pores already formed during pyrolysis, as underlined by Jacob et al. (2008). Therefore, it is critical to know specifically the type of the pores where these iron oxide nanoparticles would be accessible and more active, which remains very little addressed in the work of heterogeneous catalysis on this type of materials.

In this study, an activated carbon has been prepared in the optimum conditions from the banana spike to develop a high micromesoporosity. Further, it has been used to support iron oxide nanoparticles at different rates of wet impregnation to obtain three heterogeneous catalysts. As-prepared heterogeneous catalysts were characterized by nitrogen and carbon dioxide adsorption–desorption measurements, atomic absorption, X-ray photoelectron spectroscopy (XPS) and transmission electron microscopy (TEM). The catalysts were tested in an aqueous solution in a batch reactor for the heterogeneous Fenton degradation of Rhodamine B, a xanthene dye, used as a model dye because of its high stability and known to undergo a natural anaerobic degradation in streams yielding the production of potentially carcinogenic aromatic amines (Gao et al. 2015; Rochat et al. 1978). The influence of the dispersion of iron nanoparticles within the pores of the heterogeneous catalysts obtained at different impregnation rates was studied on the removal of Rhodamine B by adsorption and Fenton degradation. The influence of the Fenton degradation parameters, such as initial concentrations of H₂O₂ and Rhodamine B, catalyst amount, pH and temperature, was studied on the best catalyst. Removal efficiency of Rhodamine B was evaluated by the rate of discoloration of the solution, the reduction in total organic carbon (TOC) and total nitrogen (TN).

Materials and methods

Reagents

The reagents used are of analytical grade: Rhodamine B ($\geq 97\%$, Sigma-Aldrich, chemical formula C₂₈H₃₁ClN₂O₃, absorption wavelength $\lambda = 554$ nm, color index number 45,170 and dimensions: length 1.5 nm; width 0.98 nm; and thickness 0.43 nm (Canning et al. 2014)); H₂O₂ (30 wt%, Sigma-Aldrich); FeSO₄·7H₂O (99.5 wt%, Merck); NaOH (Sigma-Aldrich, 0.1 mol/L); Na₂SO₃ ($\geq 99\%$, Sigma-Aldrich); HCl (37 wt%, Sigma-Aldrich); H₃PO₄ (85 wt%, Sigma-Aldrich). pH of the Rhodamine B solutions were adjusted using 0.1 mol/L HCl or NaOH aqueous solutions. Distilled water was used to prepare the synthetic solutions of Rhodamine B as well as the other analytical solutions.

Preparation of catalysts

The micromesoporous activated carbon (AC) used to support the iron nanoparticles was obtained by chemical activation (Briton et al. 2018). Thus, three catalysts were prepared by the impregnation of AC (4 g) in iron sulfate aqueous solutions (200 mL). The iron mass percentages of the solutions in which AC was dispersed were of 3%, 7% and 11%, respectively. Each dispersion was stirred for two hours in closed Erlenmeyer flasks at 300 rpm to adsorb the Fe^{2+} ions in the AC pores. Then, the dispersions were dried both using a rotary evaporator (*Büchi Rotavapor R-200*) at 100 °C and in an oven for 1 h at 105 °C. They were further heat-treated (under oxygen limited atmosphere) at 350 °C in a muffle furnace for 2 h (heating rate of 10 °C/min). The catalysts were crushed and sieved of at 125 μm . The catalysts prepared were designated as AC@Fe/1, AC@Fe/2 and AC@Fe/3 according to the increasing iron impregnation ratios: 3%, 7% and 11%.

Characterization of the catalysts

Specific surface area and porosity of the heterogeneous catalysts were determined by using a “Micromeritics ASAP 2020” sorptometer through adsorption–desorption measurements of N_2 at 77 K and CO_2 at 273 K. The specific surface area was calculated according to the Brunauer–Emmett–Teller equation (BET) considering the relative pressure range of 0.01–0.05 as for microporous materials (Kaneko and Ishii 1992).

The pore size distributions (PSDs) were determined by fitting N_2 adsorption isotherms at 77 K and CO_2 adsorption isotherms at 273 K with, respectively, a finite slit pore model and an infinite slit pore model, calculated by the non-local functional density theory (NLDFT) (Jagiello and Olivier 2009). The volume of the supermicropores (diameter between 0.7 and 2 nm) and of mesopores was calculated from the N_2 adsorption. The volume of ultramicropores (diameter below 0.7 nm) was obtained from the PSD from CO_2 adsorption.

XPS was used to characterize the surface chemistry of the catalysts. The binding energy of the chemical elements, C, O, S, P and especially Fe, was determined in order to investigate the chemical nature of iron compound formed in the pores. XPS spectra have been obtained with an ESCALab 220i-XL (Fisons Instruments) using the $\text{AlK}\alpha$ monochromatic source and a hemispherical analyzer. Thus, high-resolution (0.1 eV) spectra have been obtained on the energy ranges 123–142 eV (P2p), 158–174 eV (S2p), 275.1–299.9 eV (C1s), 525.1–544.9 eV (O1s) and 700.1–739.9 eV (Fe2p) with a passing energy of 20 eV.

A mapping of the chemical elements of the iron-based AC@Fe/3 catalyst has been achieved using a ZEISS ULTRA 55 Gemini field emission gun scanning electron microscope

(FEG-SEM) coupled to an EDAX-type energy-dispersive spectrometer (EDS).

The TEM images of the catalysts were obtained using an EM-002B (TOPCON Co.) microscope equipped with a LaB_6 thermal filament at 120 kV acceleration voltage. For the TEM observations, the powder samples have been dispersed in water under ultrasound and then fixed on a copper grid.

DRX diagrams were obtained using the capillary powder method with the INEL diffractometer. The use of a position detector sensitive to the INEL CPS 120 curve allowed simultaneous recording of the diffracted intensity over a range of 3° – 90° 2θ with a 0.03° pitch. The radiation used is a monochromatic beam $\text{CoK}\alpha 1$.

The iron content in the catalysts was determined by atomic absorption. The catalyst was firstly calcined and its ash dissolved in 5 mL of 37 wt% HCl. Then 20 mL of distilled water were added to the solution further boiled to one-third of its volume. After cooling, the solution filtered on ordinary paper and completed to 50 mL with distilled water was analyzed using a Varian SpectrAA-20 brand flame atomic absorption spectrometer. The total iron content is evaluated relative to the mass of AC@Fe according to the following formula:

$$\% \text{Fe} = \frac{[\text{Fe}^{2+} \& \text{Fe}^{3+}] V}{m_{\text{AC@Fe}}} \times 100 \quad (1)$$

where $m_{\text{AC@Fe}}$ is the mass of AC@Fe before calcination (g), V the volume of calcined AC@Fe solution (mL) and $[\text{Fe}^{2+} \& \text{Fe}^{3+}]$ the concentration of total iron dissolved in acidic solution (mg/L).

Catalytic activity

Before testing the catalytic potential, adsorption tests were carried out to assess the Rhodamine B adsorption by the catalysts (AC@Fe/1, AC@Fe/2, AC@Fe/3). These tests were conducted without any H_2O_2 addition in the same conditions as described for the heterogeneous Fenton process.

The catalytic activity was tested through several series of experiments (operated in triplicate) in 200 mL of Rhodamine B solution at a given concentration under magnetic stirring (300 rpm) with the required doses of catalyst and H_2O_2 (30 wt%) in Erlenmeyer flasks. At the selected time, 1 mL was collected from the reaction solution and diluted in 4 mL of distilled water, and then, 0.3 mL of Na_2SO_3 (0.1 mol/L) was added to deactivate the hydroxyl radicals (Li et al. 2014). The solution was thus centrifuged with a centrifuge at 3000 rpm to recover the supernatant without fines particles and analyzed by UV–visible spectrophotometry (Cary scan 50) at 554 nm to determine the Rhodamine

B residual concentration (C) (standard range from 0 to 7 mg/L).

First the AC@Fe/1, AC@Fe/2 and AC@Fe/3 catalysts were compared for the 50 mg/L Rhodamine B removal kinetics studied at dose of 0.2 g/L, with 4 mmol/L H₂O₂, at pH 4.2 and 28 °C. In a second set of experiments, the influence of the Fenton degradation parameters on the Rhodamine B removal kinetics has been studied by using the AC@Fe/3 catalyst. Reaction parameters have been varied, such as initial concentration of H₂O₂ (from 4 mmol/L to 10 mmol/L), catalyst dose (from 0.2 g/L to 0.4 g/L), pH (from 2 to 8), Rhodamine B initial concentration (from 30 mg/L to 100 mg/L) and temperature (20 °C, 28 °C and 40 °C).

To assess the Rhodamine B mineralization, TOC and TN contents were measured by using a Shimadzu TOC-VCSN analyzer calibrated by a potassium phthalate standard solution. The iron leaching concentration in the test solution was measured by atomic absorption (Varian SpectraAA-20).

To assess the catalyst stability and the possibility of its reusing, four successive experiments of Rhodamine B (50 mg/L) discoloration kinetics were conducted on AC@Fe/3 (0.27 g/L) with 8 mmol/L H₂O₂ (pH = 4.2 at 28 °C). After each cycle, the reaction mixture was placed in an oven at 40 °C for 10 h to accelerate the regeneration of the catalyst active sites and then filtered to recover the catalyst. The catalyst particles were further washed with distilled water and dried in an oven for 2 h at 105 °C before reusing.

Results and discussion

Characterization of AC and heterogeneous catalysts

The binding energies of the chemical elements (Table 1) obtained from the XPS spectra of the AC@Fe/1, AC@Fe/2 and AC@Fe/3 catalysts have confirmed the presence of carbon, oxygen, phosphorus, iron and sulfur. In fact, the sulfur and iron contained in the catalysts originate from the iron sulfate used to impregnate AC. The carbon, oxygen and phosphorus are initially present in the raw AC. In addition, the mass percentages of the atomic elements have also been determined (Table 1). The carbon and phosphorus contents decreased in catalyst compared to pristine AC from 78.61 to 71.25% and 6.89–5.29%, respectively, while iron gradually

increased to a maximum of 2.45% (content in AC@Fe/3) on the AC surface.

The deconvolution of the Fe2p spectra (Fig. 1) of each catalyst yielded four peaks located around 711.7 eV, 715.72 eV, 724.76 eV and 728.27 eV, respectively. Thus, the major contributions at 711.7 eV and 724.76 eV are attributed

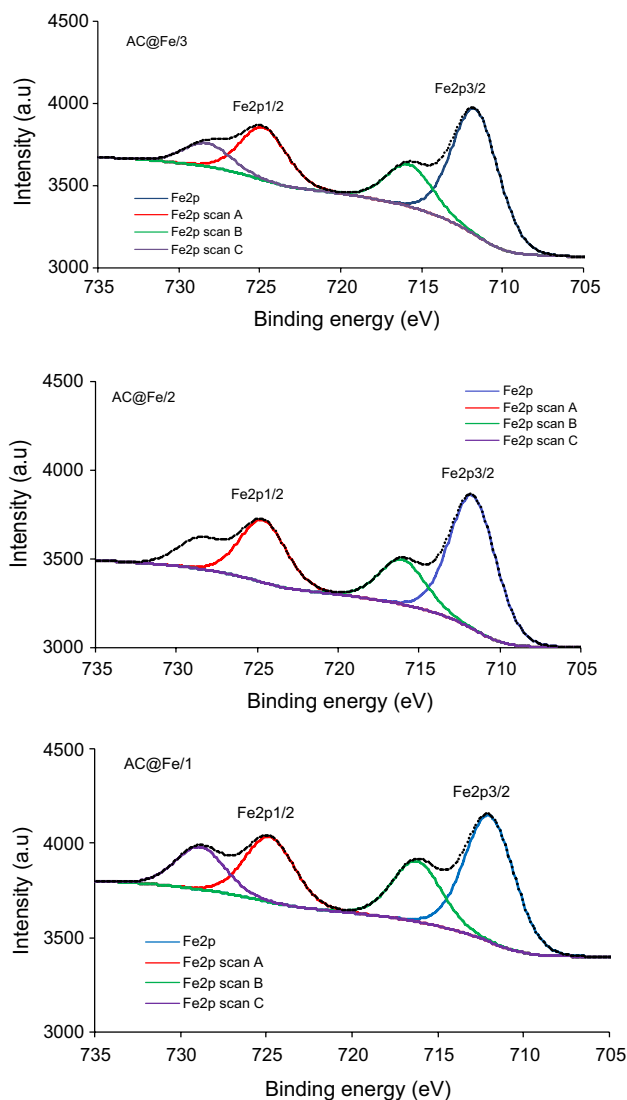


Fig. 1 Fe2p XPS spectra of AC@Fe/1, AC@Fe/2 and AC@Fe/3 catalysts

Table 1 XPS analysis results of heterogeneous catalysts and AC showing binding energies of various chemical elements and their content

	Binding energy (eV)					Chemical element (wt%)				
	C1s	O1s	P2p	Fe2p	S2p	C	O	P	Fe	S
AC	284.69	533.09	133.90	–	–	78.61	14.51	6.89	–	–
AC@Fe/1	284.72	531.43	133.76	712.01	168.76	76.10	14.77	6.40	0.80	1.93
AC@Fe/2	284.59	531.48	133.62	711.68	168.76	74.83	15.02	5.17	1.67	3.30
AC@Fe/3	284.61	531.49	133.41	711.70	168.75	71.25	15.46	5.29	2.45	5.55

to Fe2p3/2 and Fe2p1/2, respectively (Guo et al. 2019). For these three heterogeneous catalysts, the difference between the Fe2p3/2 binding energy and that of satellite peaks is around 4 eV. Indeed, these differences in binding energy are close to that obtained by Yamashita and Hayes (2008) to clearly confirm the presence of Fe²⁺. In addition, these satellites are frequently used as fingerprints to identify iron oxide phases (Pariante et al. 2008). This binding energy around of 715.72 eV indicates the presence of wüstite (FeO) (Abreu et al. 2014; Gota et al. 1999) and is typical of an iron (II) oxidation state.

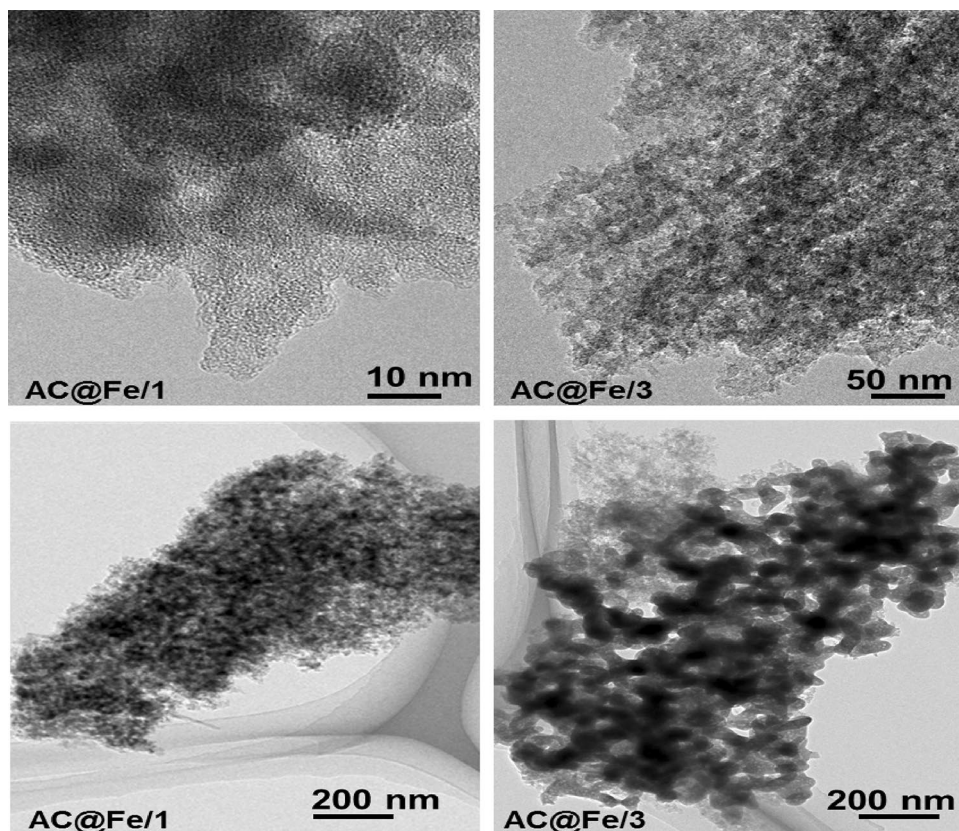
The EDAX analyses coupled to SEM mapping (Fig. S1) of the chemical elements of an iron-based nanoparticle of AC@Fe/3 catalyst have been previously described (Briton et al. 2018). They have shown that iron can be present together with O and P so that oxo-phosphate of iron might also have been formed together with iron oxides. The P element present on the surface of AC originates from the reaction of phosphoric acid with carbon during the activation of the carbon which is known to produce P–O surface functional groups (Puziy et al. 2005).

The presence of iron-based nanoparticles in all catalysts is evidenced by TEM analysis (Fig. 2). For example, TEM image displays nanoparticles of size in the range 1–50 nm remarkably dispersed in the matrix of AC@Fe/1 and AC@Fe/3 catalysts. Moreover, smaller nanoparticle sizes have

been observed in AC@Fe/1 (from about 1 nm to 10 nm) as in the iron-impregnated silica matrix prepared by Mahy et al. (2014). The variation of size observed in the AC@Fe/3 catalyst (from 1 to 50 nm) could be the result of different growth conditions because of the higher impregnation rate of this catalyst. The increase in the impregnation rate could promote the polycondensation of iron nanoparticles as reported by Karimzadeh et al. (2017). Clusters of nanoparticles are clearly highlighted in the AC@Fe/3 TEM images (at 200 nm scale). The sizes and the aspects of the observed nanoparticles are likely to suggest that they are localized in the micropores as well as in the mesopores.

XRD diagrams (Fig. 3) of AC@Fe/1, AC@Fe/2 and AC@Fe/3 catalysts each have a diffusion halo around 26.7° generally observed in activated carbons (Kan et al. 2017). The absence of diffraction peaks related to iron oxide crystallites suggests that these iron nanoparticles have been incorporated or confined in the AC pores as isolated sites and/or deposited as highly dispersed oxide species (Mazilu et al. 2017). This dispersion of iron nanoparticles within the nanopores confers on these heterogeneous catalysts an amorphous structure (Chen et al. 2009; Mazilu et al. 2017). In addition, these formed nanoparticles would be too small because the low percentages of iron in these samples do not favor net reflection corresponding to crystalline phases as

Fig. 2 AC@Fe/1 and AC@Fe/3 TEM images



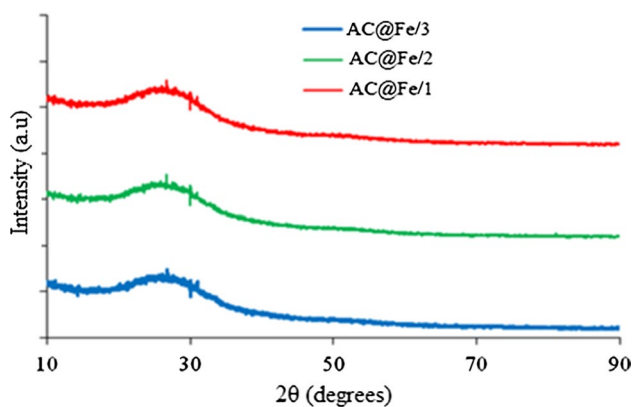


Fig. 3 XRD spectra of heterogeneous catalysts AC@Fe/1, AC@Fe/2 and AC@Fe/3

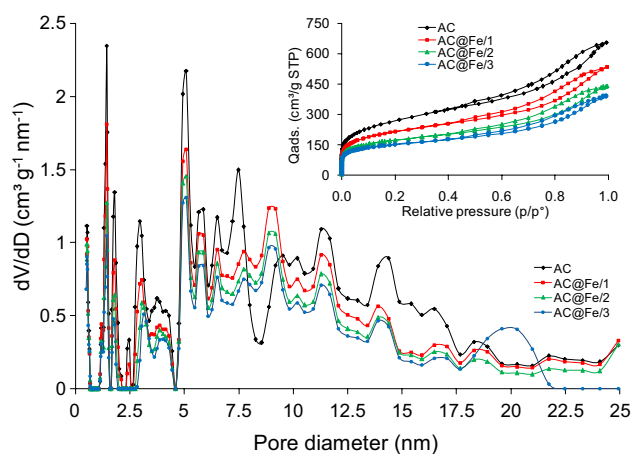


Fig. 4 AC and heterogeneous catalysts PSDs from N₂ adsorption at 77 K. Inset: N₂ adsorption–desorption isotherms of the AC support and AC@Fe/1, AC@Fe/2 and AC@Fe/3 catalysts

reported by other authors (Kadirova et al. 2013; Silva et al. 2017).

The nitrogen adsorption and desorption isotherms of inserted graph (Fig. 4) are of type IV according to the IUPAC classification and therefore typical of both microporous and

mesoporous materials. Indeed, for all isotherms, a hysteresis loop is observed between the desorption and the adsorption curves, typical of the nitrogen capillary condensation in the mesopores. Indeed, at relative pressure greater than 0.1, the isotherm adsorption profiles show a constant slope increase related to the gradual filling of the mesopores. The hysteresis loops in the relative pressure range 0.452–0.995 are of H3 type according to the IUPAC classification (Sing et al. 1982). Moreover, the PSDs (Fig. 4) confirm the presence of more or less wide slit mesopores (\varnothing from 2 to 25 nm). Narrow-slit pores such as supermicropores ($0.7 < \varnothing < 2$ nm) and ultramicropores ($\varnothing < 0.7$ nm) are also observed (Lowell et al. 2004).

However, porosity of heterogeneous catalysts is found to be affected as the rate of iron impregnation increases. This reflects the presence of iron-based nanoparticles inside the pores causing the decreases in the specific surface area from 896 to 532 m²/g and in the total pore volume from 0.886 to 0.509 cm³/g for AC and AC@Fe/3, respectively (Table 2). Indeed, the iron mass contents of 1.6%, 2.2% and 3.3% in AC@Fe/1, AC@Fe/2 and AC@Fe/3, respectively, determined by dissolution and atomic absorption are in agreement with the ones found by XPS analysis. These results are in agreement with previous work showing a reduction in the specific surface area of the porous material in which nanoparticles were dispersed (Duarte et al. 2012; Jonidi Jafari et al. 2017; Liu et al. 2017).

The histogram presented in Fig. 5 indicates the percentage of occupied porous volume with respect to the raw AC for all the catalysts depending on different pore size ranges. As the iron content increases, the filling rate of the supermicropores and mesopores estimated from the PSDs increases progressively. This is remarkable for the AC@Fe/3 catalyst with a high iron content where the reduction in supermicropore and mesopore volumes is strongly observed. This suggests that the iron nanoparticles are mainly accommodated in supermicropores and mesopores. It also suggests that iron nanoparticles are hardly formed in ultramicropores after calcinations despite high impregnation rates and that these ultramicropores are rather blocked up and not accessible in the catalysts.

Table 2 Textural properties of pristine AC and the prepared heterogeneous catalysts

	Vultra-micro ^a (cm ³ /g)	Vsuper-micro ^b (cm ³ /g)	Vmeso ^b (cm ³ /g)	Vpore ^b (cm ³ /g)	S _{BET} (m ² /g)	Fe (wt%)	PH _{pzc}
AC	0.159	0.195	0.691	0.886	896	–	5.6
AC@Fe/1	0.137	0.151	0.565	0.716	734	1.6	4.3
AC@Fe/2	0.138	0.105	0.473	0.578	599	2.2	3.1
AC@Fe/3	0.135	0.083	0.426	0.509	532	3.3	2.8

^aFrom CO₂ adsorption

^bFrom N₂ adsorption

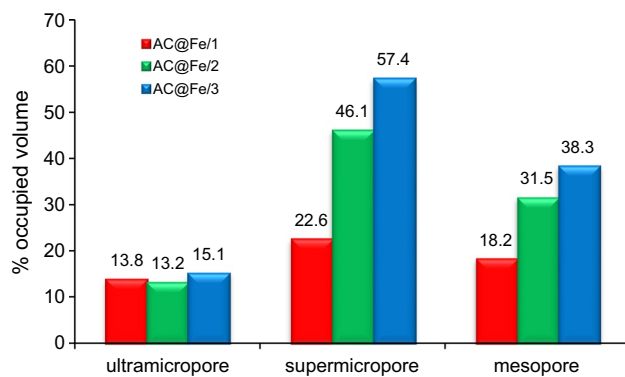


Fig. 5 Proportion of pore filling or blocking up (%) by the iron nanoparticles in the prepared heterogeneous catalysts AC@Fe/1, AC@Fe/2, AC@Fe/3 as a function of pore size range (ultramicro-pore $\varnothing < 0.7$ nm; supermicropore $0.7 \text{ nm} < \varnothing < 2$ nm; mesopore $2 \text{ nm} < \varnothing < 50$ nm) determined from the difference of the PSDs of each catalyst with respect of AC one

Removal of Rhodamine B

As adsorption is an important step in the heterogeneous Fenton oxidation process (Jonidi Jafari et al. 2017, the ability of the heterogeneous catalysts to adsorb Rhodamine B in an aqueous solution has been investigated. This adsorption is generally influenced by the media porosity and the surface chemistry (Mohammadi et al. 2010). After 180 min of contact time, the discoloring rates by adsorption are 69.2%, 59.3% and 56.1% for AC@Fe/1, AC@Fe/2 and AC@Fe/3, respectively (Fig. 6).

Rhodamine B can be present in either a cationic (positive charge on the nitrogen atom) or a zwitterionic form (positive charge on the nitrogen atom and negative charge on the oxygen of the carboxylic group) at pH value lower or higher than its pKa (3.7), respectively. At pH 4.2, the adsorption of the zwitterionic Rhodamine B on the surface of the catalysts could be favored by the presence of functional groups. The pH_{pzc} of AC@Fe/1, AC@Fe/2 and AC@Fe/3 catalysts is 4.3, 3.1 and 2.8, respectively. Thus, AC@Fe/1 is assumed to have a nearly neutral surface, while the AC@Fe/2 and AC@Fe/3 surfaces are negatively charged. These differences in the charge of the surfaces could yield different electrostatic interactions with the zwitterionic Rhodamine B, explaining the increase in the adsorption capacity as pH_{pzc} value decreases.

The strong correlation ($R^2 = 98.9\%$, inset in Fig. 6) between the adsorption capacity and the total volume of the pores reveals that the adsorption of Rhodamine B depends on the accessible porous volume. Moreover, because of its geometry and size, the Rhodamine B adsorption could occur in the mesopores and in the supermicropores of the catalysts. In conclusion, the adsorption capacities of the catalysts are related, on the one hand, to the pore volume (or the specific

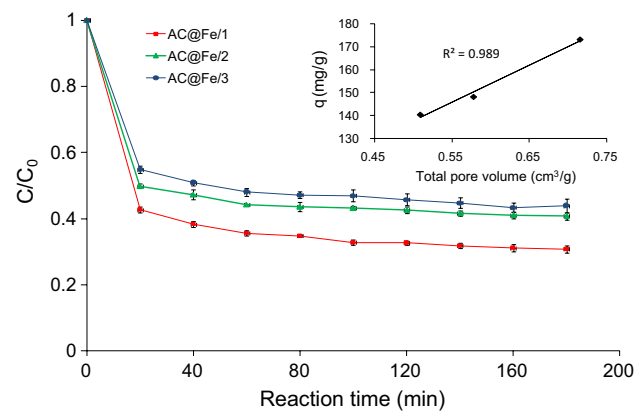


Fig. 6 Kinetics of Rhodamine B adsorption on AC@Fe/1, AC@Fe/2 and AC@Fe/3 catalysts (catalyst dose 0.2 g/L; pH 4.2; $T = 28$ °C; $C_0 = 50$ mg/L)

surface area) and, on the other hand, to the surface chemistry. Thus, as impregnation rate increases, the adsorption uptake decreases. The adsorption is quick owing to the fast diffusion of the Rhodamine B molecule into the porosity of the powdered materials, and the plateau of adsorption (quasi-equilibrium) is attained after 60 min whatever the catalyst.

Prior to any catalytic degradation test, an experiment was carried out using only H_2O_2 and the Rhodamine B solution in the same amount as for the catalytic tests (Fig. 7). This test has led to a reduction of 9.25% of Rhodamine B by oxidation after 180 min. For Fenton catalytic tests, the as-prepared catalyst and the hydrogen peroxide were added simultaneously in the Rhodamine B solution in order to generate hydroxyl radicals and to degrade the molecules of Rhodamine B adsorbed in the pore volumes. After 180 min, the discoloration rates were 78.5%, 87.4%, 93.0% for AC@Fe/1, AC@Fe/2 and AC@Fe/3, respectively. Thus, the discoloring of the Rhodamine B solution was quite accelerated by the

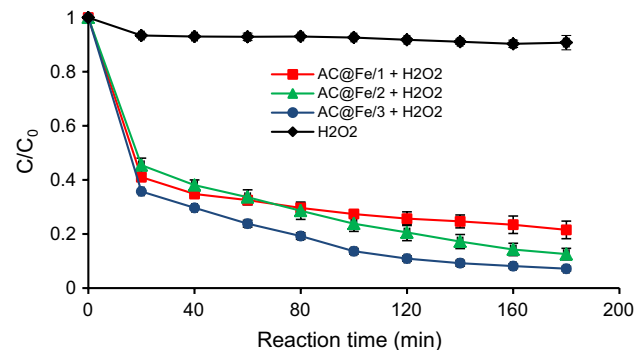


Fig. 7 Kinetics of Rhodamine B removal by heterogeneous Fenton using AC@Fe/1, AC@Fe/2 and AC@Fe/3 catalysts (catalyst dose 0.2 g/L; H_2O_2 4 mmol/L; pH 4.2; $T = 28$ °C; $C_0 = 50$ mg/L)

catalytic oxidation combined to adsorption. The profile of the kinetics of removal of Rhodamine B clearly indicates the superimposition of two phenomena. The first one is clearly adsorption which is rapid as previously observed and for which equilibrium is nearly attained after 60 min (Fig. 7), and the second one is the degradation of the Rhodamine B via Fenton reaction which continues still after the adsorption equilibrium. Indeed, Ramirez et al. (2007) reported that the mesopores are more accessible to macromolecules such as dyes, while the micropores are easily accessible to the H_2O_2 . In addition, previous studies have shown that catalyst having appropriate PSD can accelerate the degradation speed of the pollutant (Jonidi Jafari et al. 2017; Liu et al. 2017; Zhou et al. 2014). The efficiency of our prepared catalyst is thus attributed to its mesoporous/microporous PSD. As reported by Georgi and Kopinke (2005), the main degradation route is assumed to be the HO^\bullet attack on the organic fraction of dissolved contaminants in the pores of the catalytic support. In fact, the catalytic activity of iron-based nanoparticles and their dispersion within the pores appear to be the key factors for the Rhodamine B discoloration. The content in iron-based nanoparticles dispersed in the AC pores is also a critical point for the optimization of the Fenton catalyst. In previous works, the authors used relatively important doses of catalyst in order to improve the catalytic yield (Cuiping et al. 2012; Guo et al. 2017; Wang et al. 2014). Despite its low adsorption capacity, AC@Fe/3 has the best catalytic activity, due to its highest amount of iron nanoparticles dispersed in the porosity. Similarly, the Fenton catalytic efficiency of highly dispersed iron nanoparticles was also

emphasized by Li et al. (2015) and then by Mazilu et al. (2017) in non-carbonaceous materials.

Influence of reaction parameters

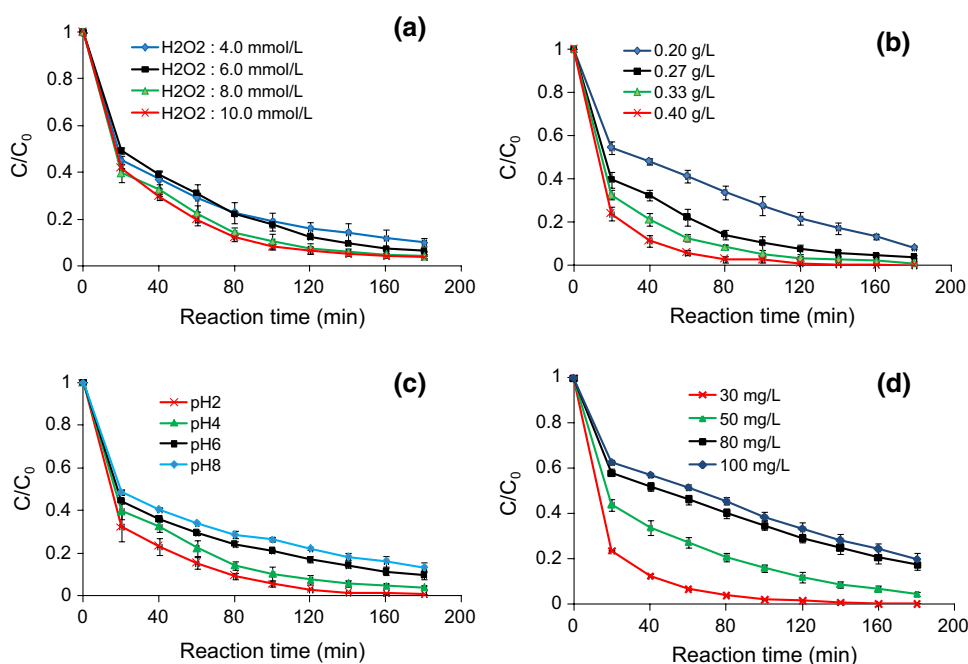
The influence of the parameters (H_2O_2 dose, catalyst dose, rhodamine B initial concentration, pH and temperature) on heterogeneous Fenton process has been studied using AC@Fe/3 as the best catalyst.

Thus, Fig. 8a shows that the Rhodamine B removal rate is increased from 90.1 to 96.4% after 180 min as the H_2O_2 dose is increased from 4 to 10 mmol/L. In fact, the increase in the H_2O_2 concentration led to a strong production of hydroxyl radicals. In addition, between 8 mmol/L and 10 mmol/L, the gap in terms of the degradation rate is of little significance. The reason is that excess of H_2O_2 reacts with HO^\bullet radicals transforming them into hydroperoxyl radicals (HO_2^\bullet) according to the following equations (Khataee et al. 2015; De Laat and Le 2006):



Those radicals [$E_0(HO_2^\bullet/H_2O) = 1.7$ V] are less reactive than the HO^\bullet ones ($E_0(HO^\bullet/H_2O) = 2.8$ V). Such reactions reduce the collision probability between Rhodamine B and HO^\bullet and decrease the HO_2^\bullet degradation speed (Guo et al. 2014). The 8 mmol/L concentration is appropriate to accelerate the Rhodamine B degradation and to minimize the H_2O_2 consumption cost.

Fig. 8 Effect various parameters on the removal kinetics of Rhodamine B catalyzed by AC@Fe/3: **a** H_2O_2 concentration at pH=4.2 and 28 °C, $C_0=50$ mg/L, 0.27 g/L of catalyst, **b** effect of the catalyst dose at pH=4.2 and 28 °C, $C_0=50$ mg/L, 8 mmol/L of H_2O_2 , **c** effect of pH at 28 °C, $C_0=50$ mg/L, 0.27 g/L of catalyst, 8 mmol/L of H_2O_2 , **d** effect of the Rhodamine B initial concentration at pH=4.2 and 28 °C, 0.27 g/L of catalyst, 8 mmol/L of H_2O_2



The effect of the catalyst dose (from 0.20 to 0.40 g/L) studied on the discoloration of a 50 ppm Rhodamine B solution (Fig. 8b) displays the acceleration of removal kinetics as increasing the catalyst amount. Indeed, the obtained rates are 92.0%, 96.1%, 99.2% and 100% for a dose of 0.20 g/L, 0.27 g/L, 0.33 g/L and 0.40 g/L, respectively. Comparison with previous works shows that higher dose of 1 g/L of iron-loaded silicate (3 wt% Fe) (Gan and Li 2013) and 50 g/L iron-loaded graphite (15 wt% Fe) (Cuiping et al. 2012) were used to discolor 5 mg/L and 100 mg/L Rhodamine B solutions, respectively. This proves the efficiency of the AC@Fe/3 prepared catalyst. Indeed, as the catalyst dose increases, the number of active sites also increases to generate a significant amount of hydroxyl radicals attacking the Rhodamine B chromophore groups. This attack can be also favored by the adsorption owing to a large contact surface availability on the catalyst.

Figure 8c shows that the discoloring rate decreases at the beginning of the removal kinetics as the pH increases: Rates are 99.4%, 96.1%, 90.2% and 86.6% for pH 2.0, 4.2, 6.2 and 8.2, respectively. Thus, the pH increase yields a decrease in the adsorption capacity of the catalysts. Previous authors reported that the Rhodamine B adsorption on activated carbon was optimal at pH lower than the pKa (3.7) of Rhodamine B (Guo et al. 2005; Mohammadi et al. 2010) where the adsorbate global charge is positive. Thus, this molecule could be electrostatically attracted by the negatively charged surface of the catalyst (at $\text{pH} > \text{pH}_{\text{pzc}}$ where $\text{pH}_{\text{pzc}} = 2.8$). At pH higher than 3.7, the deprotonation of the carboxyl group occurs giving the zwitterionic form of Rhodamine B (Gan and Li 2013; Guo et al. 2005) which may increase its aggregation in forms of dimers by electrostatic interactions between the xanthenes and the carboxyl groups of monomers (Gad and El-Sayed 2009; Guo et al. 2005). This dimerization reduces the adsorption on the catalyst active sites. Also, at pH above pKa (3.7), the emergence of COO^- functional group in the zwitterionic form promotes some electrostatic repulsion in the presence of negatively charged catalyst ($\text{pH}_{\text{pzc}} = 2.8$). The decomposition of hydrogen peroxide into molecular oxygen without formation of any significant amount of hydroxyl radicals could also explain the decrease in the degradation rate as pH rises (Chen et al. 2010; Guo and Al-Dahhan 2003). Though pH 2 gives the highest rate (99.4% in Fig. 8c), an iron leaching of 2.892 mg/L is observed. At pH 4.2, 6 and 8, the Fe leaching rates are 0.507 mg/L, 0.142 mg/L and 0.100 mg/L, respectively.

As increasing the initial concentration from 30 to 100 mg/L, the discoloration rate turned from 100 to 80% after 180 min (Fig. 8d). Indeed, the increase in the Rhodamine B concentration could cause a congestion of the active sites by hindering the contact of the hydrogen peroxide and the catalyst and yielding a less effective oxidation reaction

of the Rhodamine B. In fact, the discoloring can be more and more delayed due to a large number of molecules of Rhodamine B and intermediate compounds to degrade (Cuiping et al. 2012; Murugananthan et al. 2008). 80% of removal at $C_0 = 100$ mg/L demonstrates the catalytic potential of AC@Fe/3 which is expected to respond to any variation of dye concentration in the wastewater.

The kinetics of discoloration is increased together with the temperature in the range 20–40 °C (Fig. 9). The degradation rate varies from 76.2 to 99.04% after 180 min of treatment, as increasing the temperature from 20 to 40 °C. The temperature increase favors the production of hydroxyl radicals accelerating the Rhodamine B degradation. The value of the k constant rate (estimated from the slope of $\ln(C/C_0)$ versus time plot) (Matouq et al. 2014) determined from the pseudo-first-order kinetics fits rises from 0.006 min^{-1} at 20 °C to 0.030 min^{-1} at 40 °C. According to the Arrhenius law (Eq. 4), the activation energy E_a is deduced (Hites 2017):

$$\ln k = \ln A - \frac{E_a}{RT} \quad (4)$$

where A is pre-exponential factor, E_a is the energy of activation (J/mol), R is the perfect gas constant (8.314 J/mol/K) and T is the absolute temperature (K).

The 55.2 kJ/mol calculated activation energy is roughly between 60 and 250 kJ/mol as for advanced oxidation reactions (Chen and Zhu 2007). Also, this agrees with the 82.5 kJ/mol activation energy reported by Gan and Li (2013) for the Rhodamine B oxidation catalyzed by iron supported on silica.

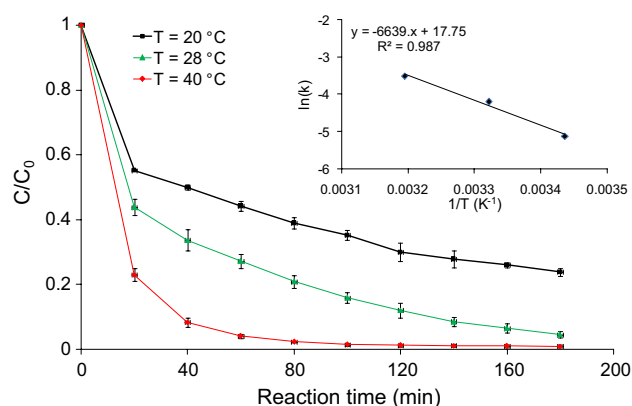


Fig. 9 Effect of temperature on the discoloration of the Rhodamine B and the Arrhenius law representation as inset ($\ln(K)$ versus $1/T$): AC@Fe/3 0.27 g/L; $C_0 = 50$ mg/L; $\text{pH} = 4.2$; 8 mmol/L H_2O_2

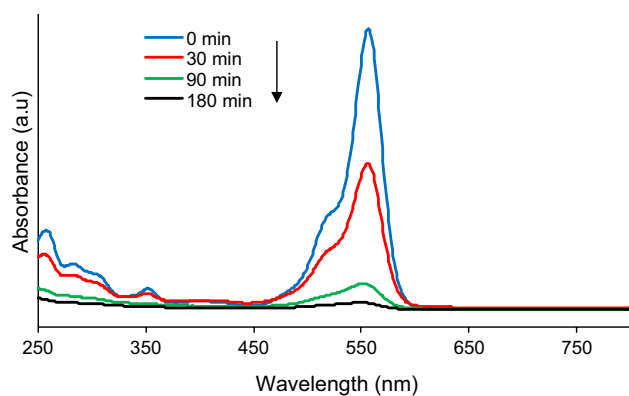


Fig. 10 Spectral variation of Rhodamine B during treatment ($C_0=50$ mg/L and 28 °C, pH=4.2; AC@Fe/3 0.27 g/L; 8 mmol/L of H_2O_2)

Mineralization and Rhodamine B spectral variation

The UV–visible absorption spectra (Fig. 10) of the solutions collected at different times during the Rhodamine B removal kinetics by using AC@Fe/3 present three absorption peaks. The high-intensity peak at 554 nm is assigned to the extended chromophore, comprising all the coupled aromatic cycles connected by the C=C and C=N double bonds, while the peaks at 347 nm and 252 nm reveal the presence of cyclic benzene structure of Rhodamine B (Hou et al. 2011). During the treatment, an intensity reduction affects all the peaks from 90 min until their quasi-total disappearance after 180 min. This reveals the destruction of chromophore groups and benzene nuclei concomitant to the Rhodamine B degradation. After 180 min, 64% TOC and 70.7% TN of the Rhodamine B solution have been converted into mineral compounds. These results are in agreement with previous work (Hadjltaief et al. 2013), showing that the discoloration is much faster than the total dye mineralization.

Stability of the catalyst

The catalyst stability study showed that its efficiency decreased from 96.1% in the first cycle to 73.3% in the fourth cycle (Fig. 11). Indeed, little decreases in efficiency of 10%, 11.3% and 0.8% were observed after the second, third and fourth cycles, respectively. This might be linked to the iron leaching in solution as highlighted by some authors (Kakavandi et al. 2016; Ramirez et al. 2007; Yang et al. 2015). The leached iron doses were 0.507 mg/L, 0.476 mg/L and 0.4 mg/L, after the first, second and third cycles, respectively, explained by the slight leaching of the iron nanoparticles within the pores (loss of 15.7% of iron between the first and the fourth cycles).

The decrease in the catalytic activity is related to the loss of iron from the catalyst and could be also due to the

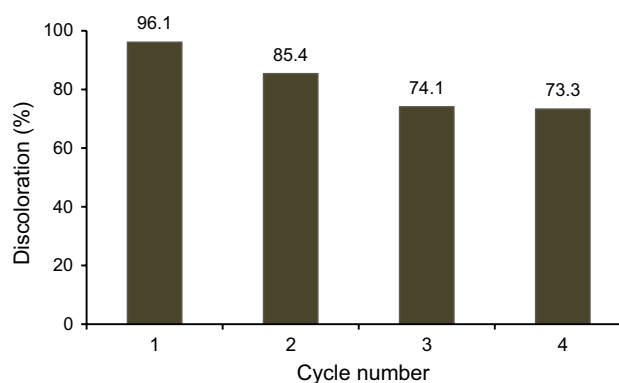


Fig. 11 Repeated recycling of AC@Fe/3 (0.27 g/L) with H_2O_2 (8 mM) for the degradation of Rhodamine B (50 mg/L) (pH=4.2, Temperature = 28 °C)

deactivation of the catalytic sites. BET surface area of the used catalyst was found to be almost similar to the pristine (from 534 to 511 m^2/g after the second cycle) revealing almost no change in the pore occupancy. Though the activity of the catalyst has decreased to some extent, it has a potential for reuse as its stability is strongly related to the dispersion of the iron oxide nanoparticles through the pores. Considering the work of Rubeena et al. (2018), this low concentration of leached iron during each cycle is not responsible for the degradation of Rhodamine B, but this degradation rather results from the iron nanoparticles dispersed within the pores. In addition, this dose of dissolved iron is slightly greater than the dose of iron in the tap water recommended (WHO 2011). Therefore, the rejection of this solution of Rhodamine B treated with this catalyst does not present an environmental pollution risk.

After the degradation of Rhodamine B, XPS analysis was performed on AC@Fe/3 catalyst already used to obtain information on the degree of chemical oxidation of the iron nanoparticles after generating hydroxyl radicals in the presence of peroxide. Thus, from the comparison of Fe2p spectra before and after catalytic tests (Fig. 12), it can be observed a modification on the spectrum marked by a displacement of the satellite peak toward Fe2p_{1/2}. According to the literature, this satellite peak located at 718.42 eV reflects the presence of iron nanoparticles in the form Fe₂O₃ (Beswick et al. 2015; Wang et al. 2013). This indicates that a fraction of Fe(II) of the wüstite (FeO) was converted to Fe(III) during the heterogeneous Fenton reaction.

In this study, catalyst stability and degradation reactions are mainly attributed to the dispersion of iron nanoparticles into micropores and mesopores. Indeed, micropores that are not very accessible to Rhodamine B, but rather to H_2O_2 molecules, guarantee the stability of heterogeneous catalyst to sustain the production of hydroxyl radicals. Thus, through the mesopores more accessible to Rhodamine

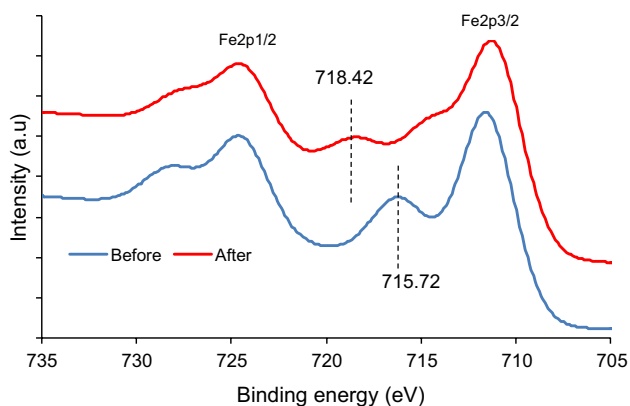


Fig. 12 XPS spectra of AC@Fe/3 catalyst before and after the degradation of Rhodamine B

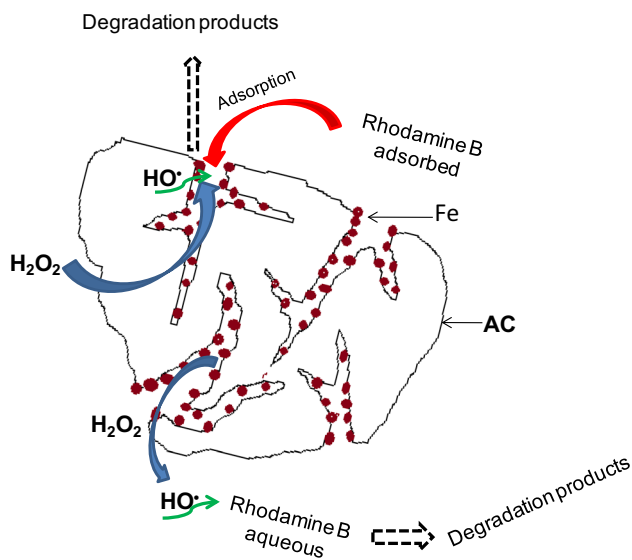


Fig. 13 Mechanism of Rhodamine B degradation using a heterogeneous catalyst in the presence of H_2O_2

B, the hydroxyl radicals generated in both micropores and mesopores will degrade the previously adsorbed dye. In parallel, a part of the hydroxyl radicals oxidizes in an aqueous media the dye located near the active sites. This leads us to propose a mechanism of the degradation of this dye mainly in the mesopores of the heterogeneous catalyst (Fig. 13).

Conclusion

Some heterogeneous catalysts for Fenton oxidation were prepared by the iron sulfate solution impregnation at different ratios of an activated carbon from banana spike further pyrolyzed at 350 °C. AC@Fe/1, AC@Fe/2 and AC@Fe/3 catalysts have been obtained with different amounts

of iron-based nanoparticles (3, 7 and 11 wt% of Fe/AC ratio, respectively), containing O and P, mainly localized in supermicropores and mesopores as observed by XPS, TEM, SEM and PSD from N_2 and CO_2 adsorption. These heterogeneous catalysts were tested for the oxidation of Rhodamine B solution by the Fenton process in the presence of H_2O_2 . AC@Fe/3 is the most promising catalyst explained by the high dispersion of iron (II)-based nanoparticles in the activated carbon nanopores. In addition, the influence of factors such as the temperature, pH, catalyst dose, H_2O_2 concentration and initial dye concentration has been studied to define the optimized conditions for the Rhodamine B removal kinetics when using the AC@Fe/3 catalyst. Using this catalyst (0.27 g/L at pH 4.2) with 8 mmol/L H_2O_2 , an important abatement rate of the target pollutant (Rhodamine B, $C_0 = 50$ mg/L) was obtained such as a 96.1% discoloring rate and 64% TOC reduction after 180 min. The solution discoloration is due to the Rhodamine B degradation and its mineralization as 70.7% of nitrogen has been removed and the benzene rings observed through spectral variation have disappeared. After the second cycle, the catalytic performance remained almost constant and around 73%. After four successive tests, a 15.7 wt% iron loss of this catalyst was observed. The residual presence of iron indicates that the catalyst remains potentially active for further Fenton reactions. In fact, this catalyst could be used to treat some real textile effluents by their dye degradation.

Acknowledgements The authors thank French Embassy in Côte d'Ivoire via Campus-France and Agence Universitaire de la Francophonie for awarding the PhD scholarship to *Bi Gouessé Henri Briton*.

Funding This work was not funded by a donor.

Compliance with ethical standards

Conflict of interest The authors declare that they have no conflict of interest.

Ethical approval The authors certify that article is original work that has not been published elsewhere and approve the submission to Applied Water Science.

Informed consent All authors have endorsed the publication of this research.

Open Access This article is distributed under the terms of the Creative Commons Attribution 4.0 International License (<http://creativecommons.org/licenses/by/4.0/>), which permits unrestricted use, distribution, and reproduction in any medium, provided you give appropriate credit to the original author(s) and the source, provide a link to the Creative Commons license, and indicate if changes were made.

References

- Abreu GJP, Paniago R, Pfannes HD (2014) Growth of ultra-thin FeO(100) films on Ag(100): a combined XPS, LEED and CEMS study. *J Magn Magn Mater* 349:235–239. <https://doi.org/10.1016/j.jmmm.2013.08.059>
- Ahmadi M, Kakavandi B, Jorfi S, Azizi M (2017) Oxidative degradation of aniline and benzotriazole over PAC@Fe^{II}Fe^{III}O₄: a recyclable catalyst in a heterogeneous photo-Fenton-like system. *J Photoch Photobiol A* 336:42–53. <https://doi.org/10.1016/j.jphotochem.2016.12.014>
- Bačić G, Mojović M (2005) EPR spin trapping of oxygen radicals in plants: a methodological overview. *Ann Ny Acad Sci* 1048:230–243. <https://doi.org/10.1196/annals.1342.021>
- Baldrian P, Merhautová V, Gabriel J, Nerud F, Stopka P, Hrubý M, Beneš MJ (2006) Decolorization of synthetic dyes by hydrogen peroxide with heterogeneous catalysis by mixed iron oxides. *Appl Catal B-Environ* 66:258–264. <https://doi.org/10.1016/j.apcatb.2006.04.001>
- Beswick O, Yuranov I, Alexander DTL, Kiwi-Minsker L (2015) Iron oxide nanoparticles supported on activated carbon fibers catalyze chemoselective reduction of nitroarenes under mild conditions. *Catal Today* 249:45–51. <https://doi.org/10.1016/j.cattod.2015.01.023>
- Briton BGH, Duclaux L, Richardson Y, Yao KB, Reinert L, Soneda Y (2018) Optimization of total organic carbon removal of a real dyeing wastewater by heterogeneous Fenton using response surface methodology. *Desalin Water Treat* 136:186–198. <https://doi.org/10.5004/dwt.2018.22845>
- Canning J, Huyang G, Ma M, Beavis A, Bishop D, Cook K, McDonagh A, Shi D, Peng GD, Crossley M (2014) Percolation diffusion into self-assembled mesoporous silica microfibres. *Nanomaterials* 4:157–174. <https://doi.org/10.3390/nano4010157>
- Castro CS, Guerreiro MC, Oliveira LCA, Gonçalves M, Anastácio AS, Nazzarro M (2009) Iron oxide dispersed over activated carbon: support influence on the oxidation of the model molecule methylene blue. *Appl Catal A-Gen* 367:53–58. <https://doi.org/10.1016/j.apcata.2009.07.032>
- Chen J, Zhu L (2007) Heterogeneous UV-Fenton catalytic degradation of dyestuff in water with hydroxyl-Fe pillared bentonite. *Catal Today* 126:463–470. <https://doi.org/10.1016/j.cattod.2007.06.022>
- Chen CJ, Lai HY, Lin CC, Wang JS, Chiang RK (2009) Preparation of monodisperse iron oxide nanoparticles via the synthesis and decomposition of iron fatty acid complexes. *Nanoscale Res Lett* 4:1343–1350. <https://doi.org/10.1007/s11671-009-9403-x>
- Chen Q, Wu P, Dang Z, Zhu N, Li P, Wu J, Wang X (2010) Iron pillared vermiculite as a heterogeneous photo-Fenton catalyst for photocatalytic degradation of azo dye reactive brilliant orange X-GN. *Sep Purif Technol* 71:315–323. <https://doi.org/10.1016/j.seppur.2009.12.017>
- Cuiping B, Wenqi G, Dexin F, Mo X, Qi Z, Shaohua C, Zhongxue G, Yanshui Z (2012) Natural graphite tailings as heterogeneous Fenton catalyst for the decolorization of rhodamine B. *Chem Eng J* 197:306–313. <https://doi.org/10.1016/j.cej.2012.04.108>
- De Laat J, Le TG (2006) Effects of chloride ions on the iron(III)-catalyzed decomposition of hydrogen peroxide and on the efficiency of the Fenton-like oxidation process. *Appl Catal B-Environ* 66:137–146. <https://doi.org/10.1016/j.apcatb.2006.03.008>
- De Lima Perini JA, Perez-Moya M, Nogueira RFP (2013) Photo-Fenton degradation kinetics of low ciprofloxacin concentration using different iron sources and pH. *J Photoch Photobiol A* 259:53–58. <https://doi.org/10.1016/j.jphotochem.2013.03.002>
- Dellamatrice PM, Silva-Stenico ME, Moraes LAB, Fiore MF, Monteiro RTR (2016) Degradation of textile dyes by cyanobacteria. *Braz J Microbiol* 48:25–31. <https://doi.org/10.1016/j.bjm.2016.09.012>
- Diao ZH, Xu XR, Jiang D, Li G, Liu JJ, Kong LJ, Zuo LZ (2017) Enhanced catalytic degradation of ciprofloxacin with FeS₂/SiO₂ microspheres as heterogeneous Fenton catalyst: kinetics, reaction pathways and mechanism. *J Hazard Mater* 327:108–115. <https://doi.org/10.1016/j.jhazmat.2016.12.045>
- Duarte F, Maldonado-Hódar FJ, Madeira LM (2012) Influence of the particle size of activated carbons on their performance as Fe supports for developing Fenton-like catalysts. *Ind Eng Chem Res* 51:9218–9226. <https://doi.org/10.1021/ie300167r>
- El Bouraie M, El Din WS (2016) Biodegradation of Reactive Black 5 by *Aeromonas hydrophila* strain isolated from dye-contaminated textile wastewater. *Sustain Environ Res* 26:209–216
- El-Shafey EI, Syeda NFA, Saleh AB, Haider AJAL (2016) Preparation and characterization of surface functionalized activated carbons from date palm leaflets and application for methylene blue removal. *J Environ Chem Eng* 4:2713–2724. <https://doi.org/10.1016/j.jece.2016.05.015>
- Gad HMM, El-Sayed AA (2009) Activated carbon from agricultural by-products for the removal of Rhodamine-B from aqueous solution. *J Hazard Mater* 168:1070–1081. <https://doi.org/10.1016/j.jhazmat.2009.02.155>
- Gan PP, Li SFY (2013) Efficient removal of Rhodamine B using a rice hull-based silica supported iron catalyst by Fenton-like process. *Chem Eng J* 229:351–363. <https://doi.org/10.1016/j.cej.2013.06.020>
- Gao Y, Wang Y, Zhang H (2015) Removal of Rhodamine B with Fe-supported bentonite as heterogeneous photo-Fenton catalyst under visible irradiation. *Appl Catal B-Environ* 178:29–36
- Garza-Campos B, Brillas E, Hernández-Ramírez A, El-Ghenymy A, Guzmán-Mar JL, Ruiz-Ruiz EJ (2016) Salicylic acid degradation by advanced oxidation processes. Coupling of solar photoelectro-Fenton and solar heterogeneous photocatalysis. *J Hazard Mater* 319:34–42
- Georgi A, Kopinke FD (2005) Interaction of adsorption and catalytic reactions in water decontamination processes: part I. Oxidation of organic contaminants with hydrogen peroxide catalyzed by activated carbon. *Appl Catal B-Environ* 58:9–18. <https://doi.org/10.1016/j.apcatb.2004.11.014>
- Gota S, Guiot E, Henriot M, Gautier-Soyer M (1999) Atomic-oxygen-assisted MBE growth of α -Fe₂O₃ on α -Al₂O₃(0001): metastable FeO(111)-like phase at subnanometer thicknesses. *Phys Rev B* 60:14387–14395. <https://doi.org/10.1103/PhysRevB.60.14387>
- Guo J, Al-Dahhan M (2003) Catalytic wet oxidation of phenol by hydrogen peroxide over pillared clay catalyst. *Ind Eng Chem Res* 42:2450–2460. <https://doi.org/10.1021/ie020344t>
- Guo Y, Zhao J, Zhang H, Yang S, Qi J, Wang Z, Xu H (2005) Use of rice husk-based porous carbon for adsorption of Rhodamine B from aqueous solutions. *Dyes Pigments* 66:123–128. <https://doi.org/10.1016/j.dyepig.2004.09.014>
- Guo S, Zhang G, Wang J (2014) Photo-Fenton degradation of rhodamine B using Fe₂O₃-Kaolin as heterogeneous catalyst: characterization, process optimization and mechanism. *J Colloid Interf Sci* 433:1–8. <https://doi.org/10.1016/j.jcis.2014.07.017>
- Guo S, Yuan N, Zhang G, Yu JC (2017) Graphene modified iron sludge derived from homogeneous Fenton process as an efficient heterogeneous Fenton catalyst for degradation of organic pollutants. *Micropor Mesopor Mat* 238:62–68. <https://doi.org/10.1016/j.micromeso.2016.02.033>
- Guo T, Wang K, Zhang G, Wu X (2019) A novel α -Fe₂O₃@g-C₃N₄ catalyst: synthesis derived from Fe-based MOF and its superior photo-Fenton performance. *Appl Surf Sci* 469:331–339. <https://doi.org/10.1016/j.apsusc.2018.10.183>

- Hadjltaief HB, Costa PD, Galvez ME, Zina MB (2013) Influence of operational parameters in the heterogeneous photo-Fenton discoloration of wastewaters in the presence of an iron-pillared clay. *Ind Eng Chem Res* 52:16656–16665. <https://doi.org/10.1021/ie4018258>
- Hassan ME, Chen Y, Liu G, Zhu D, Cai J (2016) Heterogeneous photo-Fenton degradation of methyl orange by $\text{Fe}_2\text{O}_3/\text{TiO}_2$ nanoparticles under visible light. *J Water Process Eng* 12:52–57. <https://doi.org/10.1016/j.jwpe.2016.05.014>
- Hites RA (2017) Calculating the confidence and prediction limits of a rate constant at a given temperature from an Arrhenius equation using excel. *J Chem Edu* 94:1402–1403
- Hou MF, Liao L, Zhang WD, Tang XY, Wan HF, Yin GC (2011) Degradation of rhodamine B by $\text{Fe}(0)$ -based Fenton process with H_2O_2 . *Chemosphere* 83:1279–1283
- Imran M, Shaharouna B, Crowley DE, Khalid A, Hussain S, Arshad M (2015) The stability of textile azo dyes in soil and their impact on microbial phospholipid fatty acid profiles. *Ecotox Environ Safe* 120:163–168. <https://doi.org/10.1016/j.ecoenv.2015.06.004>
- Jagiello J, Olivier JP (2009) A simple two-dimensional NLDFT model of gas adsorption in finite carbon pores. Application to pore structure analysis. *J Phys Chem C* 113:19382–19385
- Jonidi Jafari A, Kakavandi B, Jaafarzadeh N, Rezaei KR, Ahmadi M, Akbar BA (2017) Fenton-like catalytic oxidation of tetracycline by $\text{AC@Fe}_3\text{O}_4$ as a heterogeneous persulfate activator: adsorption and degradation studies. *J Ind Eng Chem*. <https://doi.org/10.1016/j.jiec.2016.09.044>
- Kadirova ZC, Katsumata KI, Isobe T, Matsushita N, Nakajima A, Okada K (2013) Adsorption and photodegradation of methylene blue by iron oxide impregnated on granular activated carbons in an oxalate solution. *Appl Surf Sci* 284:72–79. <https://doi.org/10.1016/j.apsusc.2013.07.014>
- Kakavandi B, Takdastan A, Jaafarzadeh N, Azizi M, Mirzaei A, Azari A (2016) Application of $\text{Fe}_3\text{O}_4/\text{C}$ catalyzing heterogeneous UV-Fenton system for tetracycline removal with a focus on optimization by a response surface method. *J Photoch Photobiol A* 314:178–188
- Kan Y, Yue Q, Li D, Wu Y, Gao B (2017) Preparation and characterization of activated carbons from waste tea by H_3PO_4 activation in different atmospheres for oxytetracycline removal. *J Taiwan Inst Chem Eng* 71:494–500. <https://doi.org/10.1016/j.jtice.2016.12.012>
- Kaneko K, Ishii C (1992) Superhigh surface area determination of microporous solids. *Colloid Surface* 67:203–212. [https://doi.org/10.1016/0166-6622\(92\)80299-H](https://doi.org/10.1016/0166-6622(92)80299-H)
- Karimzadeh I, Aghazadeh M, Ganjali MR, Doroudi T, Kolivand PH (2017) Preparation and characterization of iron oxide (Fe_3O_4) nanoparticles coated with polyvinylpyrrolidone/polyethylenimine through a facile one-pot deposition route. *J Magn Magn Mater* 433:148–154. <https://doi.org/10.1016/j.jmmm.2017.02.048>
- Khataee A, Salahpour F, Fathinia M, Seyyedi B, Vahid B (2015) Iron rich laterite soil with mesoporous structure for heterogeneous Fenton-like degradation of an azo dye under visible light. *J Ind Eng Chem* 26:129–135. <https://doi.org/10.1016/j.jiec.2014.11.024>
- Li W, Wang Y, Irini A (2014) Effect of pH and H_2O_2 dosage on catechol oxidation in nano- Fe_3O_4 catalyzing UV-Fenton and identification of reactive oxygen species. *Chem Eng J* 244:1–8. <https://doi.org/10.1016/j.cej.2014.01.011>
- Li X, Liu X, Xu L, Wen Y, Ma J, Wu Z (2015) Highly dispersed Pd/PdO/ Fe_2O_3 nanoparticles in SBA-15 for Fenton-like processes: confinement and synergistic effects. *Appl Catal B-Environ* 165:79–86. <https://doi.org/10.1016/j.apcatb.2014.09.071>
- Liu W, Qian J, Wang K, Xu H, Jiang D, Liu Q, Yang X, Li H (2013) Magnetically separable Fe_3O_4 nanoparticles-decorated reduced graphene oxide nanocomposite for catalytic wet hydrogen peroxide oxidation. *J Inorg Organomet Polym* 23:907–916. <https://doi.org/10.1007/s10904-013-9863-4>
- Liu X, Yin H, Lin A, Guo Z (2017) Effective removal of phenol by using activated carbon supported iron prepared under microwave irradiation as a reusable heterogeneous Fenton-like catalyst. *J Environ Chem Eng* 5:870–876. <https://doi.org/10.1016/j.jece.2017.01.010>
- Lowell S, Shields JE, Thomas MA, Thommes M (2004) Characterization of porous solids and powders: surface area, pore size, and density. Kluwer Academic Publishers, Dordrecht, pp 13–45. <https://doi.org/10.5860/CHOICE.42-5288>
- Mahy JG, Tasseroul L, Zubiaur A, Geens J, Brisbois M, Herlitschke M, Hermann R, Heinrichs B, Lambert SD (2014) Highly dispersed iron xerogel catalysts for p-nitrophenol degradation by photo-Fenton effects. *Micropor Mesopor Mat* 197:164–173. <https://doi.org/10.1016/j.micromeso.2014.06.009>
- Matouq M, Al-Anber Z, Susumu N, Tagawa T, Karapanagioti H (2014) The kinetic of dyes degradation resulted from food industry in wastewater using high frequency of ultrasound. *Sep Purif Technol* 135:42–47. <https://doi.org/10.1016/j.seppur.2014.08.002>
- Mazilu I, Ciotonea C, Chiriac A, Dragoi B, Catrinescu C, Ungureanu A, Petit S, Royer S, Dumitriu E (2017) Synthesis of highly dispersed iron species within mesoporous (Al)-SBA-15 silica as efficient heterogeneous Fenton-type catalysts. *Micropor Mesopor Mat* 241:326–337. <https://doi.org/10.1016/j.micromeso.2016.12.024>
- Mohammadi M, Hassani AJ, Mohamed AR, Najafpour GD (2010) Removal of rhodamine b from aqueous solution using palm shell-based activated carbon: adsorption and kinetic studies. *J Chem Eng Data* 55:5777–5785. <https://doi.org/10.1021/je100730a>
- Muruganathan M, Yoshihara S, Rakuma T, Shirakashi T (2008) Mineralization of bisphenol A (BPA) by anodic oxidation with boron-doped diamond (BDD) electrode. *J Hazard Mater* 154:213–220. <https://doi.org/10.1016/j.jhazmat.2007.10.011>
- Nidheesh PV, Rajan R (2016) Removal of rhodamine B from a water medium using hydroxyl and sulphate radicals generated by iron loaded activated carbon. *RSC Adv* 6:5330–5340. <https://doi.org/10.1039/C5RA19987E>
- Pariente MI, Martínez F, Melero JA, Botas JA, Velegriki T, Xekoukoulotakis NP, Mantzavinos D (2008) Heterogeneous photo-Fenton oxidation of benzoic acid in water: effect of operating conditions, reaction by-products and coupling with biological treatment. *Appl Catal B-Environ* 85:24–32. <https://doi.org/10.1016/j.apcatb.2008.06.019>
- Puziy AM, Poddubnaya OI, Martínez-Alonso A, Suárez-García F, Tascón JMD (2005) Surface chemistry of phosphorus-containing carbons of lignocellulosic origin. *Carbon* 43:2857–2868. <https://doi.org/10.1016/j.carbon.2005.06.014>
- Rache ML, García AR, Zea HR, Silva AMT, Madeira LM, Ramírez JH (2014) Azo-dye orange II degradation by the heterogeneous Fenton-like process using a zeolite Y-Fe catalyst-Kinetics with a model based on the Fermi's equation. *Appl Catal B-Environ* 146:192–200. <https://doi.org/10.1016/j.apcatb.2013.04.028>
- Rajasimman M, Babu SV, Rajamohan N (2017) Biodegradation of textile dyeing industry wastewater using modified anaerobic sequential batch reactor—Start-up, parameter optimization and performance analysis. *J Taiwan Inst Chem E* 72:171–181. <https://doi.org/10.1016/j.jtice.2017.01.027>
- Ramirez JH, Maldonado-Hódar FJ, Pérez-Cadenas AF, Moreno-Castilla C, Costa CA, Madeira LM (2007) Azo-dye Orange II degradation by heterogeneous Fenton-like reaction using carbon-Fe catalysts. *Appl Catal B-Environ* 75:312–323. <https://doi.org/10.1016/j.apcatb.2007.05.003>
- Rochat J, Demenge P, Rerat JC (1978) Toxicologic study of a fluorescent tracer: rhodamine B. *Toxicol Eur Res* 1:23–26

- Rubeena KK, Hari Prasad Reddy P, Laiju AR, Nidheesh PV (2018) Iron impregnated biochars as heterogeneous Fenton catalyst for the degradation of acid red 1 dye. *J Environ Manage* 226:320–328. <https://doi.org/10.1016/j.jenvman.2018.08.055>
- Silva LAd, Borges SMS, Paulino PN, Fraga MA, Oliva STd, Marchetti SG, Rangel MdC (2017) Methylene blue oxidation over iron oxide supported on activated carbon derived from peanut hulls. *Catal Today* 289:237–248. <https://doi.org/10.1016/j.cattod.2016.11.036>
- Sing KSW, Everett DH, Haul RAW, Moscou L, Pierotti RA, Rouquérol J, Siemieniowska T (1982) International union of pure commission on colloid and surface chemistry including catalysis * reporting physisorption data for gas/solid systems with special reference to the determination of surface area and porosity. *Pure Appl Chem* 54:2201–2218. <https://doi.org/10.1351/pac198557040603>
- Song YL, Li JT (2009) Degradation of C.I. Direct Black 168 from aqueous solution by fly ash/H₂O₂ combining ultrasound. *Ultrason Sonochem* 16:440–444. <https://doi.org/10.1016/j.ultsonch.2008.12.011>
- Wang SH (2011) Preparation of foam concrete from graphite tailing. *Adv Mat Res* 356–360:1994–1997
- Wang Y, Zhao G, Chai S, Zhao H, Wang Y (2013) Three-dimensional homogeneous ferrite-carbon aerogel: one pot fabrication and enhanced electro-Fenton reactivity. *ACS Appl Mater Interfaces* 5:842–852. <https://doi.org/10.1021/am302437a>
- Wang X, Pan Y, Zhu Z, Wu J (2014) Efficient degradation of rhodamine B using Fe-based metallic glass catalyst by Fenton-like process. *Chemosphere* 117:638–643. <https://doi.org/10.1016/j.chemosphere.2014.09.055>
- WHO (2011) Guidelines for drinking-water quality. *World Health* 1:104–108. [https://doi.org/10.1016/S1462-0758\(00\)00006-6](https://doi.org/10.1016/S1462-0758(00)00006-6)
- Yacob AR, Majid ZA, Dasril RSD, Inderan V (2008) Comparison of various sources of high surface area carbon prepared by different types of activation. *Malays J Anal Sci* 12:264–271
- Yamashita T, Hayes P (2008) Analysis of XPS spectra of Fe²⁺ and Fe³⁺ ions in oxide materials. *Appl Surf Sci* 254:2441–2449. <https://doi.org/10.1016/j.apsusc.2007.09.063>
- Yang B, Tian Z, Zhang L, Guo Y, Yan S (2015) Enhanced heterogeneous Fenton degradation of Methylene Blue by nanoscale zero valent iron (nZVI) assembled on magnetic Fe₃O₄/reduced graphene oxide. *J Water Process Eng* 5:101–111. <https://doi.org/10.1016/j.jwpe.2015.01.006>
- Yu L, Chen J, Liang Z, Xu W, Chen L, Ye D (2016) Degradation of phenol using Fe₃O₄-GO nanocomposite as a heterogeneous photo-Fenton catalyst. *Sep Purif Technol* 171:80–87
- Zhou L, Shao Y, Liu J, Ye Z, Zhang H, Ma J, Jia Y, Gao W, Li Y (2014) Preparation and characterization of magnetic porous carbon microspheres for removal of methylene blue by a heterogeneous fenton reaction. *ACS Appl Mater Inter* 6:7275–7285. <https://doi.org/10.1021/am500576p>

Publisher's Note Springer Nature remains neutral with regard to jurisdictional claims in published maps and institutional affiliations.